Strain Engineering of Ferromagnetic-Graphene-Ferroelectric Nanostructures

Eugene A. Eliseev,[1] Anna N. Morozovska,[2,*] and Maksym V. Strikha[3,4]

[1]*Institute for Problems of Materials Science, National Academy of Sciences of Ukraine, Krjijanovskogo 3, 03142 Kyiv, Ukraine*

[2]*Institute of Physics, National Academy of Sciences of Ukraine, Pr. Nauky 46, 03028 Kyiv, Ukraine*

[3]*Taras Shevchenko Kyiv National University, Faculty of Radiophysics, Electronics and Computer Systems, Pr. Akademika Hlushkova 4g, 03022 Kyiv, Ukraine*

[4]*V.Lashkariov Institute of Semiconductor Physics, National Academy of Sciences of Ukraine, Pr. Nauky 41, 03028 Kyiv, Ukraine*

We calculate a spin-polarized conductance in a nanostructure with a composition of a "high-temperature ferromagnetic insulator-graphene-ferroelectric film," with special attention paid to control of the electric polarization direction and value in a multiaxial ferroelectric film by a misfit strain. We propose a phenomenological model, taking into account the shift of the Dirac point due to the proximity of the ferromagnetic insulator and using the Landauer formula for the conductance of the graphene channel. We derive analytical expressions, which show that the strain-dependent ferroelectric polarization governs the concentration of two-dimensional charge carriers and Fermi level in graphene in a self-consistent way. The obtained results demonstrate the opportunity to control the spin-polarized conductance of graphene by a misfit strain at room and higher temperatures in the nanostructures $CoFe_2O_4$-graphene-$PbZr_{0.4}Ti_{0.6}O_3$ and $Y_3Fe_5O_{12}$-graphene-$PbZr_{0.4}Ti_{0.6}O_3$, and thus, open up the possibilities for the application of ferromagnetic-graphene-ferroelectric nanostructures as nonvolatile spin filters and spin valves.

I. INTRODUCTION

Many efforts have been made to use organic-compatible two-dimensional graphene [1] in spintronics [2], e.g., as a nonmagnetic spacer connecting two ferromagnetic contacts of the spin valve [3–5], because spin polarization of the injection contact can be controlled by the bias and gate voltages [6]. Recently, a functional device of either a spin valve or a spin filter that uses a graphene as an active ferromagnetic element has been proposed [7]. In the device, a magnetic insulator (EuO, EuS, $CoFe_2O_4$, $Y_3Fe_5O_{12}$, or $BiFe_2O_3$) is imposed on the part of the graphene channel, resulting in the strong spin polarization of the graphene π orbitals [8–10]. The device operates due to splitting of the graphene band structure into subbands with "up" and "down" orientation of the spins, and the ferromagnetic insulator induces the energy gap between these bands [11,12]. The transition between the states of the filter and the valve is induced by the voltage applied to the bottom gate [13].

It is demonstrated experimentally [14–16] and confirmed theoretically [17,18] that a ferroelectric substrate with an out-of-plane spontaneous polarization can be used for the doping of a graphene conductive channel by a significant number of carriers without application of the gate voltage to the dielectric substrate [16,19]. Using this idea, Kurchak *et al.* [20] simulated that the nanostructure EuO-graphene-$BaTiO_3$ could operate as a spin valve at low temperatures well below the Curie temperature of EuO. However, earlier theoretical works [17,18,20] are model simulations, which do not take into consideration physical effects that are critically important for the correct understanding of the graphene-based device operation and its real applications in spintronics.

The first effect is spontaneous polarization rotation in multiaxial ferroelectrics, such as $BaTiO_3$ or $Pb(Zr, Ti)O_3$, induced by a misfit strain [21,22], originating from the lattice mismatch of the ferroelectric film and its substrate. Actually, only the out-of-plane component of the spontaneous polarization can induce a significant number of carriers in graphene, while the in-plane component does not affect the carrier density at all.

The second effect is the big (more or about 1 eV) spin-independent shift of the Dirac point induced by the proximity of a ferromagnetic insulator [8–13]. Compensation for the shift demands the mandatory presence of the

_____
*anna.n.morozovska@gmail.com

top gate [20], and consequently, precludes simulation of the "true" nonvolatile valve. Notably, the top gate is not a serious disadvantage of the EuO-graphene-BaTiO$_3$ nanostructure; the real obstacle is the strict requirement for a very small spontaneous polarization (less than mC/m^2) to move the Fermi level of graphene inside the small band gap induced by a ferromagnet. Such small polarizations possibly exist only in the immediate vicinity of the strain- or size-induced phase transitions in a thin ferroelectric film, and their values are very hard to control by, e.g., tiny changes of misfit strains.

The third effect is the low Curie temperature of EuO, $T_C = 77$ K, which prevents spin-polarized filtration at room and elevated temperatures. This obstacle can be overcome by using high-temperature ferromagnetic insulators, such as CoFe$_2$O$_4$ ($T_C = 793$ K) and Y$_3$Fe$_5$O$_{12}$ ($T_C = 550$ K), for which the proximity effects arising in the band structures of CoFe$_2$O$_4$-graphene and Y$_3$Fe$_5$O$_{12}$-graphene are calculated from first principles in Refs. [11–13].

Here, we consider the spin-dependent conductance in a poorly studied nanostructure "high-temperature ferromagnetic insulator-graphene channel-strained ferroelectric film," with special attention paid to the effects caused by the rotation of electric polarization in multiaxial ferroelectrics due to misfit strain. Our analytical calculations include a spin-independent shift of the Dirac point induced by the proximity of a ferromagnetic insulator. Using a self-consistent approach, we analyze how a strain-dependent ferroelectric polarization influences the concentration of two-dimensional charge carriers and Fermi level in graphene.

The proposed phenomenological model is presented in Sec. II, where we describe the considered geometry, discuss the effective Hamiltonian of graphene in the proximity of a ferromagnetic insulator in comparison with that of isolated graphene, analyze the Landauer formula for the conductance of the graphene channel, and study the influence of ferroelectric polarization on two-dimensional (2D) carriers in graphene. The influence of misfit strain and temperature on the Fermi energy is discussed in Sec. III. The possibility of controlling the spin-dependent conductance of the ferromagnetic-graphene-ferroelectric nanostructure by misfit strain ("strain engineering") is discussed in Sec. IV. Section V is a brief summary.

II. PHENOMENOLOGICAL MODEL

A. The geometry of the problem

A graphene single layer of length L and width W is placed between a single-domain ferromagnetic insulator and a polarized ferroelectric film of thickness h [see Fig. 1(a)]. The gap between the ferromagnet and graphene is absent to provide a maximal proximity effect. In contrast, we regard that an ultrathin dielectric gap of thickness d exists between the ferroelectric and graphene. The gap

allows the proximity effect of graphene and ferroelectric atomic wave functions to be avoided.

The out-of-plane spontaneous polarization $+P_3$ corresponds to the positive bound charge at the graphene-ferroelectric interface. The value of P_3 determines that the variation of the free carrier density in the graphene channel, namely, the proportionality $\delta\sigma \sim P_3$, exists. In fact, $|\delta\sigma| < |P_3|$, due to the electric field drop in the gap and incomplete screening of the bound charge by single-layer graphene with a very small (but finite) screening length.

B. Effective Hamiltonian of isolated graphene

A graphene honeycomb structure comprises two equivalent carbon sublattices, A and B, with charge carriers described by massless Dirac fermions. There are the two Dirac points, K and K', at the corners of the graphene Brillouin zone [see Figs. 1(b) and 1(c)]. Since the Dirac points are separated in the Brillouin zone, small perturbations cannot lift this valley degeneracy [12].

In the vicinity of these two points, $\mathbf{k} = \mathbf{K} + \mathbf{q}$ and $\mathbf{k} = \mathbf{K}' + \mathbf{q}$, the electronic structure of graphene is characterized by a linear dispersion relation with the Dirac point separating the valence and conduction bands with a zero band gap as follows:

$$H(\mathbf{q}) = \hbar v_F \mathbf{q}\hat{\sigma}. \tag{1a}$$

Here, $\hbar = 6.583 \times 10^{-16}$ eV s; $\mathbf{q}$ is the wavevector; $v_F = 10^6$ m/s represents the Fermi velocity, which does not depend on the energy or momentum; and $\hat{\sigma}$ are Pauli matrices. According to Eq. (1a), isolated single-layer graphene is a 2D gapless semiconductor with a linear band spectrum near the Dirac points:

$$E^{\pm}(q) = \pm\hbar v_F q, \tag{1b}$$

where $q = \sqrt{q_x^2 + q_y^2}$ is the momentum measured relative to the Dirac point and the signs "+" and "−" correspond to the conduction (electron) and valence (hole) bands, respectively.

C. Effective Hamiltonian of graphene in the proximity of a ferromagnetic insulator

In accordance with *ab initio* calculations [11–13], the gapless spectrum, Eq. (1), of the graphene-channel section undergoes specific modifications in the proximity of a ferromagnetic insulator. In particular, graphene sublattices A and B feel different chemical environments in the proximity of a ferromagnetic insulator, which leads to inversion symmetry breaking between K and K' points and induces the spin-dependent band-gap opening. The proximity effect
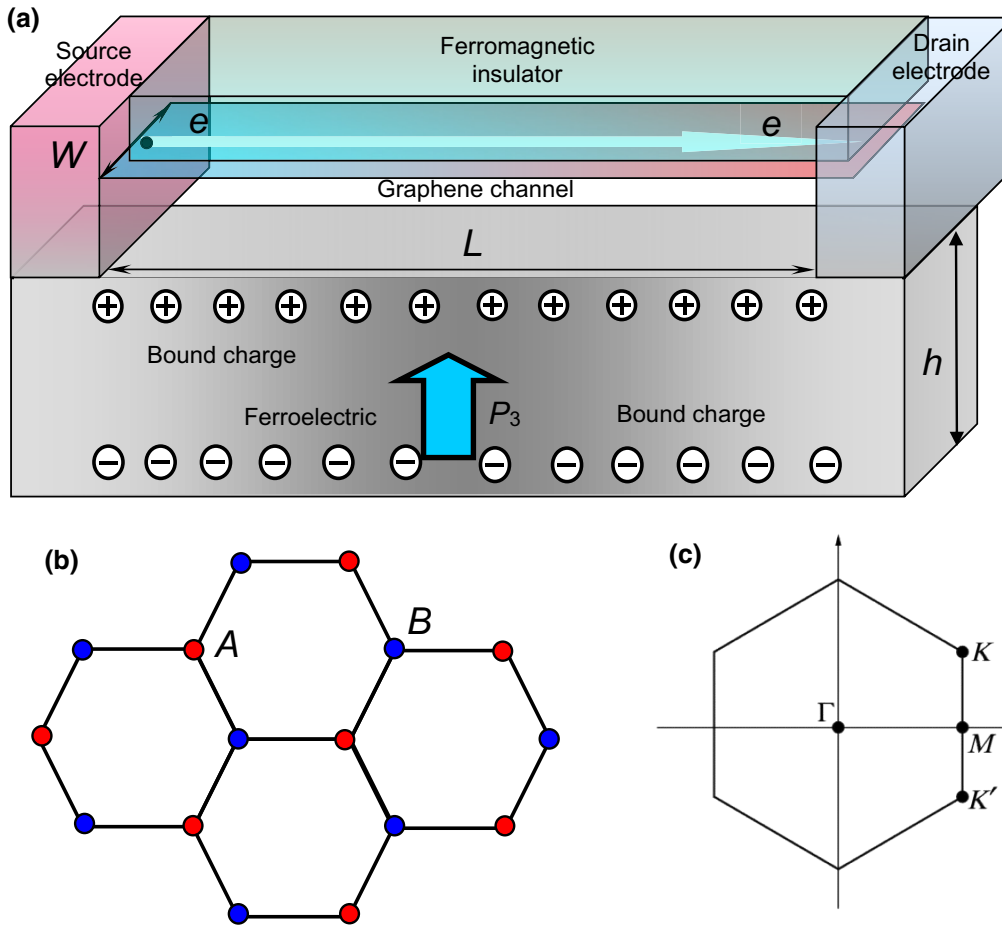
FIG. 1. (a) Graphene single layer of length L and width W is placed between a single-domain ferromagnetic insulator and a polarized ferroelectric film of thickness h. Adapted from Ref. [20]. (b) Graphene lattice with primitive vectors $\mathbf{a}_1$ and $\mathbf{a}_2$ (lattice constant 0.142 nm); marked sublattices A and B (see, e.g., Ref. [23]). (c) First Brillouin zone with marked corners K and K' of different symmetry (see, e.g., Ref. [24]).

can be modeled by the following effective Hamiltonian [13]:

$$\hat{H}_s^{\pm}(q) = \hat{\sigma}_0(D_0 + D_s) + \hbar v_s \hat{\boldsymbol{\sigma}} \mathbf{q} \pm \frac{\Delta_s}{2}\hat{\sigma}_z, \qquad (2a)$$

where the signs $+$ and $-$ correspond to K and K' valleys, respectively. The subscript $s = \uparrow, \downarrow$ designates the two values of the up and down spin projections; $\hat{\sigma}_0$ is a unit matrix; D_0 is the spin-independent shift of the Dirac point induced by the exchange coupling between the graphene sublattices and magnetic moment of magnetic atoms; $D_\uparrow$ and $D_\downarrow$ are up and down shifts of the Dirac point, respectively; and spin-dependent Fermi velocities are $v_\uparrow = 1.15 \times 10^6$ m/s and $v_\downarrow = 1.40 \times 10^6$ m/s. The spin-orbital coupling term is expressed via the Pauli matrix $\hat{\sigma}_z$. The splitting energies $\Delta_\uparrow$ and $\Delta_\downarrow$ determine the spin-dependent gap opening $(\Delta_\uparrow + \Delta_\downarrow)/2$, and the "mass" term $(\Delta_\uparrow - \Delta_\downarrow)/2$ introduced in Ref. [12].

Parameters of the effective Hamiltonian, Eq. (2a), depend on the ferromagnet material, graphene-ferromagnet lattice orientation, and on the thickness of the ferromagnetic insulator [12]. The band structure of graphene in the proximity of ferromagnetic insulators EuO, $CoFe_2O_4$, EuS, and $Y_3Fe_5O_{12}$ is calculated from first principles

[11–13]. The results [11–13] are interpolated by the analytical dependence for the energy levels [13]

$$E_s^{\pm}(q) = D_0 + D_s \pm \sqrt{(\hbar v_s q)^2 + (\Delta_s/2)^2}, \qquad (2b)$$

where the signs $+$ and $-$ correspond to the conduction (electron) and valence (hole) bands, respectively; and spin $s = \uparrow, \downarrow$. The characteristic energies of the band edges arising in the band spectrum, $E_s^{\pm}(q)$, at $q = 0$ are $E_\uparrow^{\pm}(0) = D_0 + D_\uparrow \pm (\Delta_\uparrow/2)$ and $E_\downarrow^{\pm}(0) = D_0 + D_\downarrow \pm (\Delta_\downarrow/2)$. Notably, the shift D_0 is not included in the calculations [20], and its compensation requires the presence of the top gate, and consequently, precludes modeling of the nonvolatile valve.

The dependences of the energy levels, Eq. (2), on the wave vector, $\mathbf{q}$, for $CoFe_2O_4$-graphene and $Y_3Fe_5O_{12}$-graphene nanostructures are shown in Figs. 2(a) and 2(b), respectively. Blue and red curves correspond to spin-down and spin-up states, respectively. Parameters in Eq. (2) for the pairs $CoFe_2O_4$-graphene and $Y_3Fe_5O_{12}$-graphene are listed in Table I. They are taken from *ab initio* results reported by Song *et al.* [13] and Hallal *et al.* [12], as described in Appendix A1.

One can see from Fig. 2 and Table I that the spin-dependent splitting of Landau levels, $E_g^s = E_s^+ - E_s^- \equiv \Delta_s$,
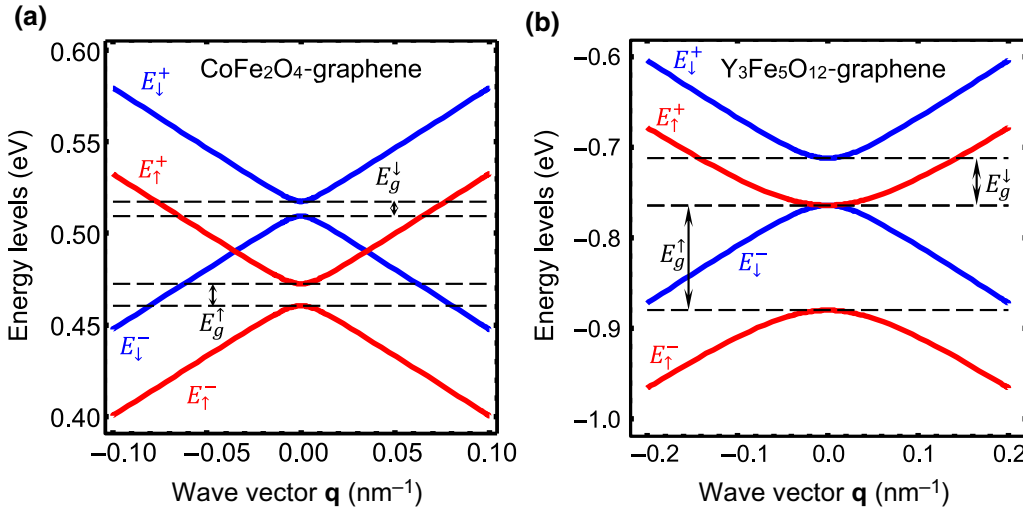
FIG. 2. Dependences of the energy levels, Eq. (2b), on wave vector **q** for $CoFe_2O_4$-graphene (a) and $Y_3Fe_5O_{12}$-graphene (b) nanostructures. Blue and red curves correspond to spin down and up states, respectively. Parameters for the pairs $CoFe_2O_4$-graphene and $Y_3Fe_5O_{12}$-graphene are listed in Table I.

is much higher for $Y_3Fe_5O_{12}$-graphene ($E_g^\uparrow = 116$ meV, $E_g^\downarrow = 52$ meV) in comparison with that of $CoFe_2O_4$-graphene ($E_g^\uparrow = 12$ meV, $E_g^\downarrow = 8$ meV). The effective masses of graphene carriers near subband edges, $m_s = \mp(\Delta_s/2v_s^2)$, are much smaller for $CoFe_2O_4$ in comparison with that of $Y_3Fe_5O_{12}$.

Hereafter, we consider a comparatively wide ($W \geq 50$ nm) and long ($L \geq 100$ nm) graphene channel fully covered with the top ferromagnetic layer and the bottom ferroelectric substrate, so edge effects are not significant. We also consider the ideal nonmagnetic electrodes (e.g., Au or Pt) that do not influence either carrier scattering in the channel or the band structure of graphene. However, the edge states should originate at any physical boundary where an electric potential drop exists (see Refs. [25–27] and reference therein). For a ferroelectric substrate, this means that our approach is applicable far from the immediate vicinity of domain walls, where the spontaneous polarization profile gradually changes its value from $-P_3$ to $+P_3$. This is possible only if we consider a single-domain ferroelectric substrate.

D. Landauer formula for the conductance of the graphene channel

The full conductance of the graphene channel, taking into account the double degeneration of graphene at points

K, K' will be described by the following modified Landauer formula [28,29]:

$$G = \sum_s G_s, \quad G_s = G_0 M_s(E_F) T_s(E_F). \qquad (3)$$

Here, the summation is over both spin values $s = \uparrow, \downarrow$. The conductance $G_0 = (e^2/2\pi\hbar)$ is the reverse Klitzing constant. $M_s(E_F)$ is the number of conductance modes; $T_s(E_F)$ is the transmission coefficient of the ferromagnetic section of length l, which is equal to the probability that the electron passes it without scattering.

The Fermi energy, E_F, is defined by the 2D concentrations of electrons, n, and holes, p, as

$$n(E_F) = \int_{-\infty}^{+\infty} g_G^+(E) f(E - E_F) dE,$$

$$p(E_F) = \int_{-\infty}^{+\infty} g_G^-(E) f(-E + E_F) dE, \qquad (4a)$$

where $f(x) = [1/1 + \exp(x/k_B T)]$ is the Fermi-Dirac distribution function, $k_B = 1.3807 \times 10^{-23}$ J/K, T is the absolute temperature, and $g_G^\pm(E)$ is the 2D density of states

TABLE I. Parameters for Eq. (2) taken from Refs. [11–13], as described in Appendix A.

Material	D_0 (eV)	$D_\uparrow$ (meV)	$D_\downarrow$ (meV)	$\Delta_\uparrow$ (meV)	$\Delta_\downarrow$ (meV)	T_C (K)	Ref.
EuO-Gr[a]	−1.36(7)	31 (33)	−31 (−33)	134	98	77	[11,13]
$Y_3Fe_5O_{12}$-Gr	−0.78	−42	+42	116	52	550	[12]
$CoFe_2O_4$-Gr	+0.49	−23.5	+23.5	12	8	793	[12]

[a]Gr, graphene.

(DOS). The DOS, derived in Appendix A.2, is

$$g_G^\pm(E) = \sum_s \int_{-\infty}^{+\infty} \frac{q\,dq}{\pi} \delta[E - E_s^\pm(q)]$$

$$= \sum_s \frac{|E - D_0 - D_s|}{\pi \hbar^2 v_s^2} H\left[\pm(E - D_0 - D_s) - \frac{\Delta_s}{2}\right],$$
$$(4b)$$

where $q = \sqrt{q_x^2 + q_y^2}$ and $H(E)$ is the Heaviside step function, $H(E > 0) = 1$ and $H(E < 0) = 0$.

Substitution of DOS Eq. (4b) into Eq. (4a) and integration lead to (see Appendix A.2)

$$n(E_F) = \sum_s \left[\frac{\Delta_s k_B T}{2\pi \hbar^2 v_s^2} \ln\left(1 + e^{\frac{E_F - D_0 - D_s - \frac{\Delta_s}{2}}{k_B T}}\right) \right.$$
$$\left. - \frac{(k_B T)^2}{\pi \hbar^2 v_s^2} \text{Li}_2\left(-e^{\frac{E_F - D_0 - D_s - \frac{\Delta_s}{2}}{k_B T}}\right) \right], \quad (4c)$$

where $\text{Li}_2(x)$ is a particular case of the polylogarithm function $\text{Li}_m(x) = \sum_{k=1}^{\infty}(x^k/k^m)$. An expression for the holes can be obtained from Eq. (4c) with the substitution $E_F \rightarrow -E_F$, $D_0 \rightarrow -D_0$, and $D_s \rightarrow -D_s$. Notably, exact analytical expression (4c) shows how the 2D concentration of carriers depends on the proximity effect [via the combination of parameters $D_0 - D_s - (\Delta_s/2)$] and on the Fermi level, E_F. Notably, the spin-dependent terms in Eq. (4c) almost coincide with corresponding terms in Eq. (74) derived by Gorbar *et al.* [30] after the shift of chemical potential on $D_0 + D_s$.

For the temperatures $k_B T \ll |E_F - D_0 - D_s \mp (\Delta_s/2)|$, the graphene charge density can be estimated as

$$e[p(E_F) - n(E_F)] \approx \frac{e}{2\pi \hbar^2} \sum_s \frac{1}{v_s^2}$$

$$\times \left[(E_F - D_0 - D_s)^2 - \left(\frac{\Delta_s}{2}\right)^2 \right] \text{sign}(D_0 + D_s - E_F).$$
$$(5)$$

It appears that Eq. (5) is accurate enough for $Y_3Fe_5O_{12}/Gr$ and $CoFe_2O_4/Gr$ parameters at temperatures $T < 350–400$ K; otherwise, we will solve Eq. (4c) for Fermi-level determination. Notably, Eq. (5) allows us to express the Fermi level, E_F, via the graphene charge density in a self-consistent manner. Notably, there is similarity between Eq. (5) and Eq. (77) in Ref. [30].

Below we assume that $M_s(E_F) = 0$ when a Fermi level is inside the energy gap of the spectrum, Eq. (2). Outside the gap, $M_s(E_F)$ is described by [29]

$$M_s = \text{int}\left[\frac{2W}{\lambda_{DB}^s}\right], \quad (6a)$$

where "int" denotes the integer part and λ_{DB}^s is the electron de Broglie wavelength:

$$\lambda_{DB}^s = \frac{2\pi}{q_s(E_F)} \approx \frac{2\pi \hbar v_s}{\sqrt{(E_F - D_0 - D_s)^2 - (\Delta_s/2)^2}}, \quad (6b)$$

where $q_s(E) = \frac{1}{\hbar v_s}\sqrt{(E - D_0 - D_s)^2 - (\Delta_s/2)^2}$ is a solution of Eq. (2b) for the given energy E, and the approximate equality is valid under the assumption $v_s \approx v_F$. The physical meaning of $M(E_F)$ for the 2D channel is the number of de Broglie half-wavelengths, which can be located at the width of this channel W.

Finally, let us analyze the transmission coefficient $T_s(E_F)$ introduced in Ref. [13]. We use here a standard Mott's two-channel model for conductance [31] and assume the hierarchy of lengths $\lambda_{AP} \ll L \ll \lambda_P$, where λ_{AP} and λ_P are the electron mean free paths for spin polarization antiparallel and parallel to spin polarization of spin majority, respectively, for a proper position of the Fermi energy. This yields to the following results in the first approximation order:

(1) for spins up $T_\uparrow(E_F) \approx 1$, if the Fermi level E_F satisfies the inequalities $E_F < D_0 + D_\uparrow - (\Delta_\uparrow/2)$ or $E_F > D_0 + D_\uparrow + (\Delta_\uparrow/2)$, and $T_\uparrow(E_F) \approx 0$, if the Fermi level satisfies the inequality $D_0 + D_\uparrow - (\Delta_\uparrow/2) < E_F < D_0 + D_\uparrow + (\Delta_\uparrow/2)$;

(2) for spin down $T_\downarrow(E_F) \approx 1$, if the Fermi level E_f satisfies the inequalities $E_F < D_0 + D_\downarrow - (\Delta_\downarrow/2)$ or $E_F > D_0 + D_\downarrow + (\Delta_\downarrow/2)$, and $T_\downarrow(E_F) \approx 0$, if the Fermi level satisfies the inequality $D_0 + D_\downarrow - (\Delta_\downarrow/2) < E_F < D_0 + D_\downarrow + (\Delta_\downarrow/2)$.

Notably, the Landauer formula, Eq. (3), describes the conductance of a structurally "perfect" (i.e., defect-free) graphene channel in a ballistic regime. Since we will use Eq. (3) for room and elevated temperatures, this means that we consider a purely ballistic transport without any scattering in the channel of length L, which is regarded smaller than that of the electron mean free path λ. The assumption requires additional discussion of its realizability. Notably, many graphene devices, especially those using graphene with structural defects or those bound to a substrate with ionized impurities, operate under ambient conditions in a diffusive or quasiballistic regime [32–34].

It is demonstrated experimentally that even a one-dimensional (1D) graphene nanoribbon can be a good ballistic conductor at low temperatures (approximately 10 K) if the 20-nm-wide device is about 100 nm long

[35]. Unlike Ref. [35], we consider electronic transport in a 2D graphene single layer for a wide temperature range of 0–400 K. However, the 1D nanoribbon, which is strongly confined in one of two lateral directions and in the out-of-plane direction, is a relevant example to demonstrate the role of edge scattering effects, which can be neglected if a graphene channel is wide enough in one lateral direction ($W \geq 50$ nm) and rather long in the other one ($L > 100$ nm); this is exactly our case. In the case of a wide 2D graphene channel, quasiballistic conductance has been observed for submicron channel lengths since 2004 (see, e.g., Ref. [1]), and a ballistic conductance for a 100–200-nm-long perfect graphene channel under ambient conditions is now a routine case (see, e.g., Ref. [32] and references therein).

To resume, edge scattering becomes unessential for the case of a comparatively wide graphene channel ($W \geq 50$ nm), and the ballistic conductivity can occur even for channel lengths of $L > 100$ nm. Actually, elementary estimations, as listed in Appendix B, demonstrate that, if the strain-free graphene channel is structurally perfect or contains negligible concentration of structural defects, and the concentration of charged impurities in a substrate is small enough, the regime of ballistic transport can be realized up to submicron-sized L because of the small intensity of scattering by acoustic phonons [32–34].

E. Influence of ferroelectric polarization on the 2D carriers in graphene

The next step is to define the density, n, of 2D carriers in graphene in a self-consistent way. Since we consider a single-domain ferroelectric film, where the electric field is constant, the surface charge, σ, stored in graphene is [36]

$$\sigma = \frac{h \, P_3}{h + d_{\text{eff}}}, \tag{7a}$$

where we introduce an effective width of dielectric gap

$$d_{\text{eff}} = \varepsilon_f \left[\frac{d}{\varepsilon_d} + \frac{l_s}{\varepsilon_G} \tanh \left(\frac{g}{l_s} \right) \right], \tag{7b}$$

and regard that single-layer graphene of effective thickness $g \sim 0.312$ nm can be characterized by the effective screening length, l_S, and dielectric permittivity, $\varepsilon_G \sim 1$ (in the direction normal to the graphene layer). The background permittivity [37] of a ferroelectric film in the out-of-plane direction is $\varepsilon_f \sim 10$. Since the length l_S of a semimetal is usually smaller (or significantly smaller) than 0.1 nm [37,38], we obtain that the inequality $l_S \ll 2g$ is characteristic for a gapless semiconductor. Since the ferroelectric film has a thickness $h \gg 2g \gg d$, the inequality $h \gg l_S$ is valid. Thus, the concentration of free carriers in graphene

acquires the form [36]

$$p - n = \frac{\sigma}{e} = \frac{h}{h + d_{\text{eff}}} \frac{P_3}{e}, \tag{8}$$

where $e = 1.6 \times 10^{-19}$ C is the electron charge and $d_{\text{eff}} \approx \varepsilon_f \left[(d/\varepsilon_d) + (l_s/\varepsilon_G) \right]$ is the effective gap thickness. For numerical estimations of d_{eff}, we can regard that an ultrathin dielectric gap has a thickness $d < 0.1$ nm and dielectric permittivity $\varepsilon_d \cong 1$.

III. INFLUENCE OF MISFIT STRAIN AND TEMPERATURE ON THE FERMI ENERGY

Within the continuous-media Landau-Ginzburg-Devonshire (LGD) approach [39], the value and orientation of spontaneous polarization, P_i, in thin ferroelectric films can be controlled by the size effect, temperature T, and misfit strain u_m, originating from the film-substrate lattice-constant mismatch [21,40]. The density of LGD free energy, the minimization of which allows us to calculate the phase diagram and polarization, has the form

$$\begin{aligned} g_{\text{LGD}} = {} & a_1(P_1^2 + P_2^2) + a_3 P_3^2 + a_{11}(P_1^4 + P_2^4) + a_{33} P_3^4 \\ & + a_{12} P_1^2 P_2^2 + a_{13}(P_1^2 + P_2^2) P_3^2 \\ & + a_{111}(P_1^6 + P_2^6 + P_3^6) + a_{112}[P_1^2(P_2^4 + P_3^4) \\ & + P_2^2(P_1^4 + P_3^4) + P_3^2(P_2^4 + P_1^4)] + a_{123} P_1^2 P_2^2 P_3^2. \end{aligned} \tag{9a}$$

The coefficients

$$\begin{aligned} a_1 = {} & \alpha_{1T}(T - T_C^f) - \frac{(Q_{11} + Q_{12})u_m}{s_{11} + s_{12}}, \quad a_3 = \alpha_{1T}(T - T_C^f) \\ & - \frac{2Q_{12}u_m}{s_{11} + s_{12}} + \frac{d_{\text{eff}}}{\varepsilon_0 \varepsilon_f (h + d_{\text{eff}})}, \end{aligned} \tag{9b}$$

$$\begin{aligned} a_{11} = {} & \alpha_{11} + \frac{s_{11}(Q_{11}^2 + Q_{12}^2) - 2Q_{11}Q_{12}s_{12}}{2(s_{11}^2 - s_{12}^2)}, \quad a_{33} = \alpha_{11} \\ & + \frac{Q_{12}^2}{s_{11} + s_{12}}, \end{aligned} \tag{9c}$$

$$\begin{aligned} a_{12} = {} & \alpha_{12} - \frac{s_{12}(Q_{11}^2 + Q_{12}^2) - 2Q_{11}Q_{12}s_{11}}{s_{11}^2 - s_{12}^2}, \quad a_{13} = \alpha_{12} \\ & + \frac{Q_{12}(Q_{11} + Q_{12})}{s_{11} + s_{12}}. \end{aligned} \tag{9d}$$

Here, T_C^f is the Curie temperature of the bulk ferroelectric, Q_{ij} are the components of the electrostriction tensor, and s_{ij} are elastic compliances. The positive coefficient

α_T is proportional to the inverse Curie-Weiss constant. When deriving Eq. (9b), we use the expression for the depolarization field inside the ferroelectric film, $E_3 = -(P_3/\varepsilon_0 \varepsilon_f)[d_{\text{eff}}/(h + d_{\text{eff}})]$.

The phase diagram of the 200 nm $PbZr_{0.4}Ti_{0.6}O_3$ film in coordinates of temperature-misfit strain, which contains the paraelectric (PE) and ferroelectric (FE) phases with out-of-plane (FE_c), in-plane (FE_a), and mixed (FE_r) orientation of the polarization vector, is shown in Fig. 3(a). The dependence of the out-of-plane polarization on the misfit strain and temperature is shown in Fig. 3(b).

Notably, the phase diagram in Fig. 3(a) differs from the diagrams calculated by Pertsev *et al.* [21] by the presence of the finite-size effect. The size-effect scale is determined by the ratio of d_{eff}/h [see Eq. (9b)] and we use $h = 200$ nm and $d_{\text{eff}} = 1$ nm in Fig. 3.

The boundaries between FE_c, FE_r, and FE_a are calculated numerically. The boundaries of PE phase instability are described by the analytical expressions $a_1 = 0$ and $a_3 = 0$, which allow the estimation of PE-FE_c and PE-FE_a transition temperatures as

$$T_{\text{PE}-\text{FE}_c}(u_m, h) \approx T_C^f \left[1 + \frac{2Q_{12}u_m}{\alpha_T T_C (s_{11} + s_{12})} \right] - \frac{1}{\alpha_T \varepsilon_0 \varepsilon_f} \frac{d_{\text{eff}}}{h + d_{\text{eff}}}, \quad (10a)$$

$$T_{\text{PE}-\text{FE}_a}(u_m, h) \approx T_C^f \left[1 + \frac{(Q_{11} + Q_{12})u_m}{\alpha_T T_C (s_{11} + s_{12})} \right]. \quad (10b)$$

Notably, only the out-of-plane component of spontaneous polarization P_3 can induce a significant number of carriers in graphene [see Eq. (8)], and the in-plane components P_1 and P_2 do not influence the carrier density. So, we should select those misfit strains, u_m, and film thicknesses, h, for which the FE_c or FE_r phases with nonzero P_3 are stable at the working temperature. Meanwhile, PE and FE_a phases with $P_3 = 0$ do not present any interest for the spin-polarization effect.

It is seen from Figs. 3(a) and 3(b) that the $PbZr_{0.4}Ti_{0.6}O_3$ film should be strained with $u_m < 0.1\%$ to increase the region of stable FE_c or FE_r phases up to room and elevated temperatures. Also, the temperature stability of FE_c and FE_r phases increases as the strain decreases and becomes highest at $u_m < -1\%$. This happens because compressive strain ($u_m < 0$) increases $T_{\text{PE}-\text{FE}_c}(u_m, h)$, and tensile strain ($u_m > 0$) decreases it, since $Q_{12} < 0$ and $s_{11} + s_{12} > 0$ for $PbZr_{0.4}Ti_{0.6}O_3$ (see Table II).

Under the temperature-limiting conditions and assuming that $v_s \approx v_F$, the approximate expression for the Fermi energy should be found from the equation

$e[p(E_F) - n(E_F)] + \sigma = 0$:

$$E_F(\sigma) \approx D_0 + \frac{D_\uparrow + D_\downarrow}{2}$$
$$+ \sqrt{\frac{\Delta_\uparrow^2 + \Delta_\downarrow^2}{8} - \left(\frac{D_\uparrow - D_\downarrow}{2}\right)^2 + \frac{\pi \hbar^2 v_F^2 \sigma}{e}}. \quad (11)$$

Equation (11) is valid when $|E_F - D_0 - D_\uparrow| \gg (\Delta_\uparrow/2)$, $|E_F - D_0 - D_\downarrow| \gg (\Delta_\downarrow/2)$, and $\sigma = [h P_3(T, u_m, h)/h + d_{\text{eff}}]$, in accordance with Eq. (7a). It is seen from Eq. (11) that only the out-of-plane component of polarization, $P_3(T, u_m, h)$, can change the Fermi energy.

Notably, Eq. (11) significantly benefits from the expression $E_F = \hbar v_F \sqrt{\pi n}$, as used in Ref. [20] for this case, since it accounts for the proximity effect, polarization rotation, and depolarization effect in the presence of the dielectric gap, Eq. (7b). Not less important is that, since the charge density σ is defined by the strain-dependent polarization $P_3(T, u_m, h)$, Eq. (11) shows that the ferroelectric polarization governs the Fermi level $E_F(\sigma)$ in a self-consistent manner. Analytical expression (11) is not previously derived.

The dependences of the Fermi energy and de Broglie wavelength on the misfit strain and temperature are shown in Figs. 3(c) and 3(d), respectively. It is seen that misfit strain makes it possible to control E_F and λ_{DB} values in FE_c or FE_r phases up to room and higher temperatures; in that temperature range, the phases increase with compressive strain increase. Actually, we can vary the values of E_F and λ_{DB} in the range of $0 - 2.3$ eV and $0 - 5$ mm, respectively, by a proper choice of u_m and T [see the gradient color regions of FE_c and FE_r phases, which are separated by a slightly visible boundary in Figs. 3(c) and 3(d)]. The trianglelike violet region in Fig. 3(c) and the white region in Fig. 3(d) are the PE or FE_a phases, where the in-plane ferroelectric polarization corresponding to FE_a phase (or its absence in PE phase) cannot change E_F and λ_{DB} in graphene. It should be noted that the difference between $\lambda_{\text{DB}}^\downarrow$ and $\lambda_{\text{DB}}^\uparrow$ turns out to be insignificant for both considered nanostructures (less than 10%), and therefore, Fig. 3(d) shows only one of these two quantities.

IV. THE SPIN-DEPENDENT CONDUCTANCE OF FERROMAGNETIC-GRAPHENE-FERROELECTRIC NANOSTRUCTURE

A. Spin polarization of the nanostructure

The spin-polarization coefficient, R, is defined as [13]

$$R = \frac{G_\uparrow - G_\downarrow}{G_\uparrow + G_\downarrow}. \quad (12)$$

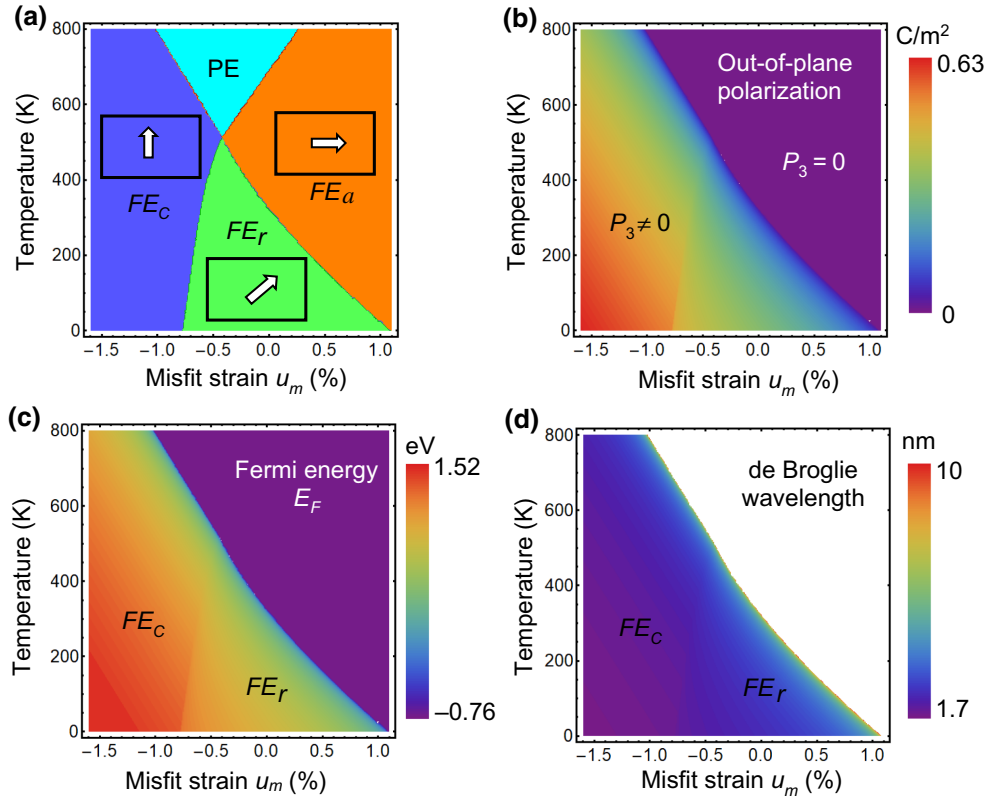FIG. 3. (a) Phase diagram of the $PbZr_{0.4}Ti_{0.6}O_3$ film polarization in coordinates of temperature-misfit strain, which contains the PE and ferroelectric phases with the out-of-plane (FE_c), in-plane (FE_a), and mixed (FE_r) orientation of the polarization vector. Dependences of the out-of-plane polarization (b), Fermi energy (c), and de Broglie wavelength (d) on the misfit strain and temperature. Color bars show the range of corresponding values at the contour maps; white arrows inside empty rectangles show the polarization direction in the film. Film thickness is $h = 200$ nm and effective gap width if $d_{eff} = 1$ nm. LGD parameters are listed in Table II.

The temperature dependence of the spin up and down graphene channel conductivities, $G_\downarrow$ and $G_\uparrow$, and spin polarization R are calculated for $CoFe_2O_4$-graphene-$PbZr_{0.4}Ti_{0.6}O_3$ [Figs. 4(a)–4(c)] and $Y_3Fe_5O_{12}$-graphene-$PbZr_{0.4}Ti_{0.6}O_3$ [Figs. 4(d)–4(f)] nanostructures. Curves 1–3 in Fig. 4 correspond to three different values of misfit strain. The temperature dependence of the conductivities $G_\downarrow$ and $G_\uparrow$ are steplike in the temperature range corresponding to the FE phase of the 200 nm $PbZr_{0.4}Ti_{0.6}O_3$ film. The spin-polarization effect disappears in the FE_a and PE phases. The steps become longer as the temperature decreases.

One can see that the $CoFe_2O_4$-graphene-$PbZr_{0.4}Ti_{0.6}O_3$ system demonstrates very narrow temperature windows for a value of $R = \pm 1$ (100% spin polarization). In fact, these values are pinned to the temperature ranges with a fraction-of-Kelvin-order width. This can make operation of the system as a spin filter unstable; however, by controlling the temperature shift within several K range, we can obtain a promising spin valve, which switches at the defined temperature from 0% to 100% spin polarization

and almost immediately to 0% polarization again. Zero values of spin polarization R are shown in the $\log_{10}$ scale in Fig. 4(c), since the temperature dependence of R has the form of a step function, and R is equal to zero in some temperature ranges. On the contrary, the $Y_3Fe_5O_{12}$-graphene-$PbZr_{0.4}Ti_{0.6}O_3$ system demonstrates the absence of temperature windows with a value of $R = 0$, which makes it promising both as a stable spin filter and as a spin valve. It should be noted that the sign of R is defined by the sign of spontaneous polarization in the single-domain ferroelectric film. This fact can open up the possibilities to modulate R using a ferroelectric film with a domain structure, which is not considered in this work.

Notably, the electrons in the small-bias linear-response case, as examined here, are injected with Fermi energy, which is approximately the same in both the graphene channel and the source and drain terminals (we treat the quasiequilibrium case). The position of the Fermi level in the graphene channel is governed by ferroelectric polarization. This control can be nontrivial, but realizable in practice.

TABLE II.   Parameters of $PbZr_{0.4}Ti_{0.6}O_3$ used in LGD phenomenological modeling from Ref. [41].

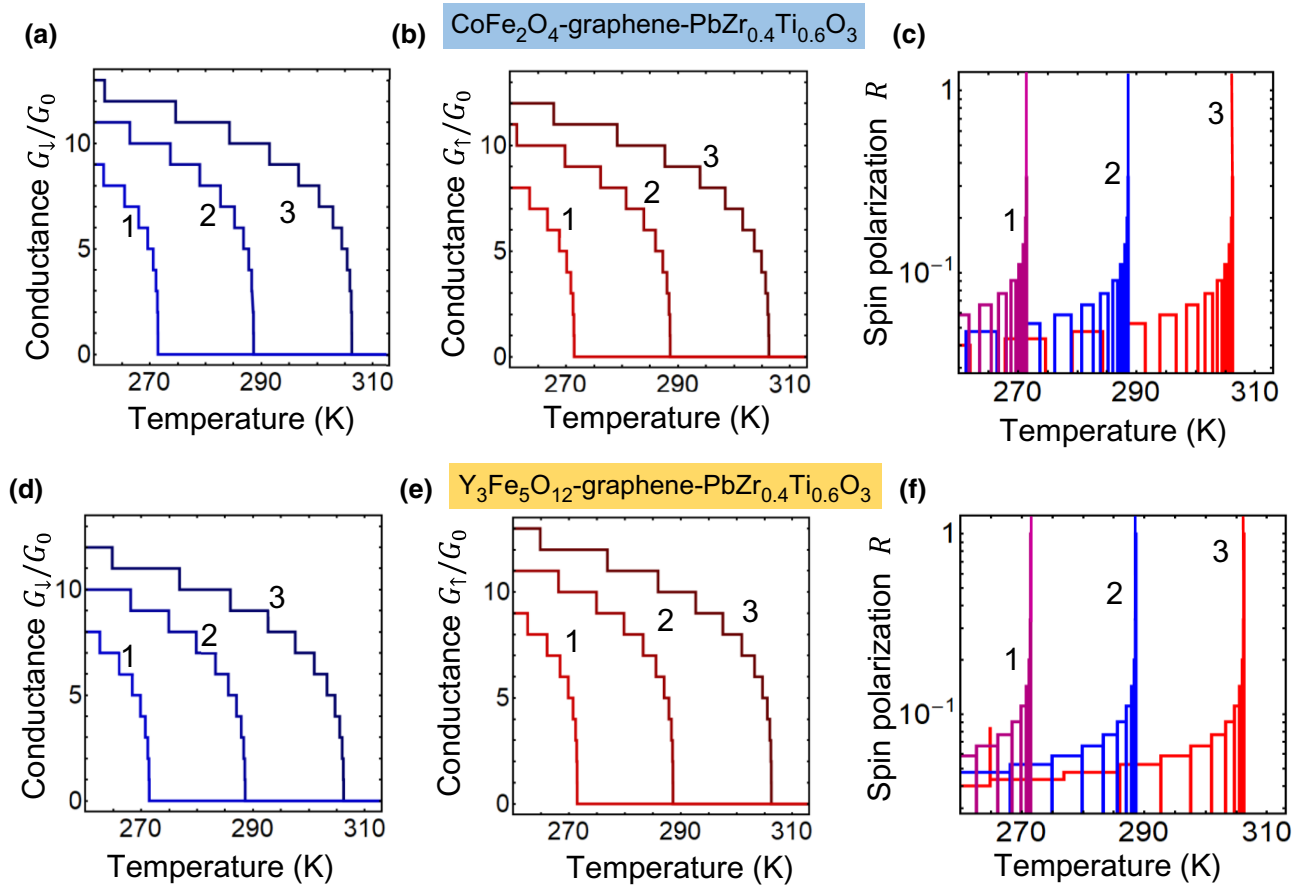| α_{1T} (10^5 m/FK)	T_C^f (°C)	α_{11} (10^7 m^5/FC^2)	α_{12} (10^8 m^5/FC^2)	a_{111} (10^8 m^9/FC^4)	a_{112} (10^8 m^9/FC^4)	a_{123} (10^9 m^9/FC^4)	Q_{11} (10^2 m^4/C^2)	Q_{12} (10^2 m^4/C^2)	Q_{44} (10^2 m^4/C^2)
2.121	418.4	3.614	3.233	1.859	8.503	−4.063	8.116	−2.950	6.710

FIG. 4. Temperature dependence of the graphene channel conductivities $G_\downarrow$ (a),(d) and $G_\uparrow$ (b),(e), and absolute value of spin polarization R (c),(f) calculated for $CoFe_2O_4$-graphene-$PbZr_{0.4}Ti_{0.6}O_3$ (a)–(c) and $Y_3Fe_5O_{12}$-graphene-$PbZr_{0.4}Ti_{0.6}O_3$ (d)–(f) nanostructures. Curves 1–3 correspond to several values of misfit strain, namely, $u_m = 1.5$, 1, and 0.5×10^{-3}, respectively. Width of the graphene channel is $W = 50$ nm, film thickness is $h = 200$ nm, and gap width is $d_{eff} = 1$ nm. Conductance is normalized on $G_0 = e^2/2\pi\hbar$. Parameters for energy levels are listed in Table I. Ferroelectric parameters are listed in Table II.

B. Strain engineering of spin polarization

The dependence of the spin polarization, R, on temperature and misfit strain calculated for the $CoFe_2O_4$-graphene-$PbZr_{0.4}Ti_{0.6}O_3$ and $Y_3Fe_5O_{12}$-graphene-$PbZr_{0.4}Ti_{0.6}O_3$ nanostructures is shown in Fig. 5(a) and 5(b), respectively. For both nanostructures, one can see two trianglelike regions with $R = 0$ separated by a thin-line-like region with maximal spin polarization $|R| = 1$. To reach $R = \pm 1$ at room temperature, strain $u_m \approx (0.07 - 0.09)\%$ should be applied to a 200-nm-thick $PbZr_{0.4}Ti_{0.6}O_3$ film. The strain becomes smaller at higher temperatures. The region with spin polarization $R \to 1$ is very narrow in the phase diagram, and it is localized near the vanishing curve of the out-of-plane component of ferroelectric polarization P_3. Far from this curve, the values of spin polarization are in the order of 0.1.

In fact, Fig. 5 demonstrates the realistic possibilities of controlling the spin-polarized conductance of graphene by a misfit strain (strain engineering) from low (<100 K) to room (approximately 300 K) and higher temperatures

$(350 - 550$ K) in the $CoFe_2O_4$-graphene-$PbZr_{0.4}Ti_{0.6}O_3$ and $Y_3Fe_5O_{12}$-graphene-$PbZr_{0.4}Ti_{0.6}O_3$ nanostructures. This makes the systems under consideration promising candidates for the fabrication of alternative spin valves and spin filters.

C. Possible experimental realization, advantages, and disadvantages of the proposed device

It is necessary to estimate the spin-scattering length for possible experimental realization of the proposed device operating due the ferromagnetic-graphene-ferroelectric nanostructure. It is well known that theory predicts spin lifetimes of about 1 μs for pristine graphene, while experiments give values ranging from tens of ps to a few ns (see, e.g., Ref. [42] and references therein). This suggests that the source of spin relaxation is of extrinsic origin (e.g., impurities, defects, static ripples). In the presence of a ferromagnetic insulator on graphene, these times can be in the ps range because of the strong spin-orbit
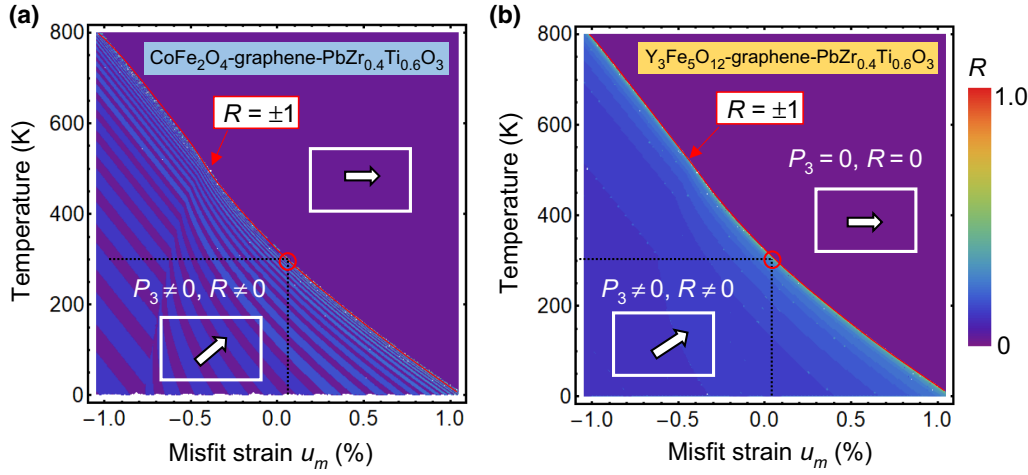
FIG. 5. Dependence of spin polarization R on temperature and misfit strain calculated for (a) $CoFe_2O_4$-graphene-$PbZr_{0.4}Ti_{0.6}O_3$ and (b) $Y_3Fe_5O_{12}$-graphene-$PbZr_{0.4}Ti_{0.6}O_3$ nanostructures. Parameters are the same as those in Figs. 3 and 4.

coupling of Rashba type [43]. The spin-scattering (or spin-flop) length, λ_{SF}, can be estimated as a product of the spin lifetime, τ_{SF}, and Fermi velocity, v_F, in graphene: $\lambda_{SF} = \tau_{SF}v_F$. Therefore, for $\tau_{SF} = 10^{-12}$ s, we get $\lambda_{SF} = 1\,\mu$m. Notably, the spin-relaxation time is related to the momentum-relaxation time, τ_p, by the approximate relation $\tau_{SF} \approx \tau_p/b^2$, where b is the amplitude of a spin admixture. Its value can be estimated as the ratio of the intrinsic spin-orbit coupling energy, $\varepsilon_I \sim (\Delta_\uparrow - \Delta_\downarrow)$, and Fermi energy, $b \approx \varepsilon_I/E_F$. Notably, for the reasons discussed in Ref. [44], the inequality $\tau_p^P > \tau_p^{AP}$ takes place for the time of momentum relaxation for the spin polarization parallel (τ_p^P) and antiparallel (τ_p^{AP}) to the polarization of spin majority for a proper position of the Fermi energy. This occurs when the inequality $\tau_{SF} \gg \tau_p^P > \tau_p^{AP}$ is valid (in the other case, the spin polarization is destroyed earlier than momentum polarization occurs). This inequality does not impose any serious restrictions on the channel length, which can be in the order of 100 nm to provide ballistic conductivity for $\tau_p \sim 10^{-13}$ s, typical for a well-fabricated graphene.

It is generally accepted that graphene is a weak spin-orbit coupling material and is generally not expected to induce a sufficient Dzyaloshinskii-Moriya interaction to affect magnetic chirality (see, e.g., Ref. [45]). However, it has been demonstrated recently by Yang [46] that, in fact, graphene can induce a type of Dzyaloshinskii-Moriya interaction due to the Rashba effect [43] in the systems "graphene on Ni or Co ferromagnetic metal." In our work, we study a somewhat different situation in the ferromagnetic insulator-graphene-ferroelectric system. If we treat a graphene channel as a rigid 2D system, the Rashba effect is absent, because of the Ehrenfest theorem [since the electronic motion in the out-of-plane direction, z, is confined to the 2D graphene channel, and the time-averaged electric field (including that of the potential that binds it to the 2D graphene surface) that the electron experiences must also be zero]. The Rashba effect, in this case, can

be nonzero in the second order of perturbation theory only, which is beyond the scope of our paper. The only limitation imposed here is that the spin-flopping length (which can be of micron order in graphene, see, e.g., Refs. [3–5]) is much longer than that of the graphene channel length (approximately 100–200 nm in our case).

The above estimations demonstrate that the studied ferromagnetic-graphene-ferroelectric nanostructure has a potential for operation in a ballistic regime as a spin valve or a spin filter. However, one should ask if this structure has any advantages for applications in comparison with existing "ferromagnetic-graphene" prototypes, where the Fermi energy to the gap regime of spin-up or spin-down subbands is switched by a voltage applied to the background gate.

The main difference of the ferroelectric substrate, in comparison with a background gate, is its nonvolatility, because the direction of spontaneous polarization in the ferroelectric film is nonvolatile and can be stored for a very long time without application of an external field [47,48]. The electric field induced in graphene by a nonvolatile polarized film plays the same role as that of a back gating. One needs to apply an electric field to change the polarization direction only, i.e., to erase existing or to record subsequent information, while nondestructive read-out is also possible due to effective surface screening [47,48]. Other differences of the ferroelectric substrate are the potential opportunities for further miniaturization of the device, because the bistable nanodomain structures can be recorded in thin ferroelectric films [48]. A multi-axial ferroelectric substrate (such as $PbZr_{0.4}Ti_{0.6}O_3$) with electric polarization rotation allows the creation of multibit memory, due to switching between more than two (up and down) directions of polarization, such as the parallel "0" direction, and more exotic vortex-type or skyrmion-type polarization states [49].

To make the above discussion balanced, we should note that control of the carrier concentration in graphene by

a gate voltage has many advantages in comparison with our proposal. First, it can be implemented easily in existing field-effect transistor technologies. However, the strain control of ferroelectric polarization, as examined in this work, has its own advantages, as described above. The main difference is that our proposal can be used in fast nonvolatile devices and, therefore, it can be considered as an alternative to electric field control by a back gate.

V. CONCLUSION

We calculate a spin-polarized conductance in the high-temperature ferromagnetic insulator-graphene-ferro electric film nanostructure, with special attention being paid to the impact of electric polarization rotation in a strained multiaxial ferroelectric film. The rotation and value of the polarization vector are controlled by a misfit strain.

The proposed phenomenological model takes into account the shift of the Dirac point induced by the proximity of a ferromagnetic insulator. We use the Landauer formula for the conductance of the graphene channel, where strain-dependent ferroelectric polarization governs the concentration of two-dimensional charge carriers and the Fermi level in graphene in a self-consistent manner. Notably, our theory permits analytical expressions for conductance and concentration to be obtained, which make further examination physically clear.

There is one essential restriction imposed on the graphene channel length in such a device: it should be shorter than the electron mean free path for spin polarization parallel to the one in the graphene channel modified by a ferromagnetic insulator and longer than the electron mean free path for spin polarization antiparallel to the one in the graphene channel. However, because of the long spin-flip length in a standard graphene-on-substrate (up to several μm scale) material, this restriction does not lead to ultrashort channels.

We demonstrate opportunities to control the spin-polarized conductance of graphene by misfit strain (strain engineering) at room and higher temperatures in the $CoFe_2O_4$-graphene-$PbZr_{0.4}Ti_{0.6}O_3$ and $Y_3Fe_5O_{12}$-graphene-$PbZr_{0.4}Ti_{0.6}O_3$ nanostructures. Namely, temperature and strain ranges exist, where spin polarization of the systems under consideration can switch from 0% to 100% and then to 0% again. The obtained results open up the possibilities for the application of ferromagnetic-graphene-ferroelectric nanostructures as nonvolatile spin filters and spin valves operating at room and higher temperatures.

ACKNOWLEDGMENTS

APPENDIX A: FERROMAGNETIC-GRAPHENE-FERROELECTRIC PARAMETERS AND DOS

1. Parameters used in Eq. (2c)

The parameters used in Eq. (2c) and listed in Table I for several FM-Gr pairs are recalculated from Hallal *et al.* [12], using the effective Hamiltonian, by the following procedure:

$$\hat{H}_{\text{eff}}^{\pm}(q) = \hbar v_F \hat{\boldsymbol{\sigma}} \mathbf{q} \mathbf{I_s} + \frac{\delta}{2} \mathbf{I_s} \hat{s}_z + \frac{\Delta_D}{2} \hat{\sigma}_z \mathbf{I_s} + \frac{\Delta_\delta}{2} \hat{\sigma}_z \hat{s}_z, \quad \text{(A1)}$$

where $\boldsymbol{\sigma}$ and $\mathbf{s}$ are the Pauli matrices that act on the sublattice and spin, respectively. The second term represents the exchange coupling induced by the magnetic moment of magnetic atoms, with $\delta = (\delta_e + \delta_h)/2$, where δ_h and δ_e are the strength of exchange spin splitting of the hole and electron, respectively. The third term results from the fact that graphene sublattices A and B are now feeling different potentials, which result in a spin-dependent band gap opening at the Dirac point, $\Delta_D = (\Delta_\uparrow + \Delta_\downarrow)/2$. The fourth term is proportional to the spin-dependent mass constant $\Delta_\delta = \frac{\delta_e - \delta_h}{2} = \frac{\Delta_\uparrow - \Delta_\downarrow}{2}$.

The characteristic energies of the band edges $[E_s^{\pm}(q) - D_0]$ arising in the band spectrum at $q = 0$ in the proximity of a ferromagnetic insulator are $D_\uparrow - \frac{\Delta_\uparrow}{2}$, $D_\uparrow + \frac{\Delta_\uparrow}{2}$, for spins up, and $D_\downarrow - (\Delta_\downarrow/2)$, $D_\downarrow + (\Delta_\downarrow/2)$, for spins down. Thus, $[D_\uparrow + (\Delta_\uparrow/2)] - [D_\downarrow + (\Delta_\downarrow/2)] = \delta_e$ and $[D_\uparrow + (\Delta_\uparrow/2)] - [D_\downarrow + (\Delta_\downarrow/2)] = \delta_h$. Hence, $2(D_\uparrow - D_\downarrow) = 4D_\uparrow = \delta_e + \delta_h$ and $\Delta_\uparrow - \Delta_\downarrow = \delta_e - \delta_h$, and thus, $D_{\uparrow,\downarrow} = \pm(\delta_e + \delta_h)/4$.

The effective Hamiltonian of Song *et al.* [13] is

$$\hat{H}_s^{\pm}(q) = \hat{\sigma}_0(D_0 + D_s) + \left(\hbar v_s \hat{\sigma} q \pm \frac{\Delta_s}{2} \hat{\sigma}_z\right), \quad \text{(A2a)}$$

where the signs "$\pm$" correspond to K and K' valleys, respectively; $s = \uparrow, \downarrow$ is the up or down spin, respectively; and the Pauli matrices are $\hat{\sigma}_0 = \begin{pmatrix} 1 & 0 \\ 0 & 1 \end{pmatrix}$, $\hat{\sigma} = (\hat{\sigma}_x, \hat{\sigma}_y)$, $\hat{\sigma}_x = \begin{pmatrix} 0 & 1 \\ 1 & 0 \end{pmatrix}$, $\hat{\sigma}_y = \begin{pmatrix} 0 & -i \\ i & 0 \end{pmatrix}$, and $\hat{\sigma}_z = \begin{pmatrix} 1 & 0 \\ 0 & -1 \end{pmatrix}$. Since $\mathbf{q} = (q_x, q_y)$, we obtain the scalar product $\hat{\sigma}q = \begin{pmatrix} 0 & q_x - iq_y \\ q_x + iq_y & 0 \end{pmatrix}$ and $\Delta_s \hat{\sigma}_z = \begin{pmatrix} \Delta_s & 0 \\ 0 & -\Delta_s \end{pmatrix}$.

The evident form of the effective Hamiltonian matrix is

$$\hat{H}_s^{\pm}(q) = \begin{pmatrix} D_0 + D_s \pm \frac{\Delta_s}{2} & \hbar v_s(q_x - iq_y) \\ \hbar v_s(q_x + iq_y) & D_0 + D_s \mp \frac{\Delta_s}{2} \end{pmatrix}. \quad \text{(A2b)}$$

Only either upper or lower signs matter simultaneously in Eq. (A2b). The eigenvalues, E_s [energy levels of Hamiltonian (A2a)], of the matrix (A2b) can be found from

$$(D_0 + D_s - E_s)^2 - \left(\frac{\Delta_s}{2}\right)^2 - (\hbar v_s)^2(q_x^2 + q_y^2) = 0. \quad \text{(A2c)}$$

The solution of Eq. (A2c) gives the analytical dependence for the energy levels as

$$E_s^{\pm}(q) = D_0 + D_s \pm \sqrt{(\hbar v_s q)^2 + (\Delta_s/2)^2}, \quad \text{(A2d)}$$

where the signs $+$ and $-$ correspond to the electrons and holes, respectively, and $s = \uparrow, \downarrow$.

Corresponding effective masses of graphene carriers, m_s, can be found from the expansion of Eq. (A2d) at small **q**, $E_s^{\pm}(q) - D_0 - D_s \approx \pm(\Delta_s/2)\{1 + (1/2)(2\hbar v_s q/\Delta_s)^2\} = \pm(\Delta_s/2) \pm (2v_s^2/\Delta_s)[(\hbar q)^2/2]$, as $m_s = \mp(\Delta_s/2v_s^2)$. Thus, $E_s^{\pm}(q) - D_0 - D_s \approx \pm(\Delta_s/2) + [(\hbar q)^2/2m_s]$.

2. DOS derivation

$$g_G^{\pm}(E) = 2\sum_s \int_{-\infty}^{+\infty} \frac{dq_x dq_y}{(2\pi)^2} \delta[E - E_s^{\pm}(q)] \equiv \sum_s \int_0^{+\infty} \frac{qdq}{\pi} \delta[E - E_s^{\pm}(q)], \quad \text{(A3a)}$$

where $\mathbf{q} = \{q_x, q_y\}$ and $q = \sqrt{q_x^2 + q_y^2}$, and degeneracy of K and K' values gives a factor of two. Using the property $\int_{-\infty}^{+\infty} \delta[a(q)]b(q)dq = \sum_i [b(q_i)/|a'(q_i)|]$ of the Dirac-delta function $\delta[q]$, where $a'(q) = da/dq$, is the derivative, we obtain from Eq. (4b)

$$g_G^+(E) = \sum_s \frac{q_s}{\pi} \left|\frac{dq_s}{dE_s^+}\right| H\left(E - D_0 - D_s - \frac{\Delta_s}{2}\right), \quad \text{(A3b)}$$

$$g_G^-(E) = \sum_s \frac{q_s}{\pi} \left|\frac{dq_s}{dE_s^-}\right| H\left(-E + D_0 + D_s - \frac{\Delta_s}{2}\right), \quad \text{(A3c)}$$

where $q_s(E) = \frac{1}{\hbar v_s}\sqrt{(E - D_0 - D_s)^2 - (\Delta_s/2)^2}$ is the positive solution of Eq. (A2b) for the given energy E, and $H(E)$ is the Heaviside step function $H(E > 0) = 1$ and $H(E < 0) = 0$. The step function appears in the DOS expression, since the equations $E = E_s^+(q)$ and $E = E_s^-(q)$ have the physical solution $q > 0$ only for the cases $E > D_0 + D_s + (\Delta_s/2)$ and $E < D_0 + D_s - (\Delta_s/2)$, respectively.

Using the expressions for the derivatives $[dE_s^{\pm}(q)/dq] = \left[\pm(\hbar v_s)^2 q/\sqrt{(\hbar v_s q)^2 + (\Delta_s/2)^2}\right]\Big|_{q=q_s} \equiv [(\hbar v_s)^2 q_s/E - D_0 - D_s]$, or the inverse derivative $dq_s/dE = [E - D_0 - D_s/(\hbar v_s)^2 q_s]$, we obtain from Eq. (A3b) the following expressions:

$$g_G^+(E) = \sum_s \frac{|E - D_0 - D_s|}{\pi \hbar^2 v_s^2} H\left(E - D_0 - D_s - \frac{\Delta_s}{2}\right) \equiv \sum_s \frac{\sqrt{(\hbar v_s q_s)^2 + (\Delta_s/2)^2}}{\pi \hbar^2 v_s^2} H\left(E - D_0 - D_s - \frac{\Delta_s}{2}\right), \quad \text{(A4a)}$$

$$g_G^-(E) = \sum_s \frac{|E - D_0 - D_s|}{\pi \hbar^2 v_s^2} H\left(D_0 + D_s - \frac{\Delta_s}{2} - E\right) \equiv \sum_s \frac{\sqrt{(\hbar v_s q_s)^2 + (\Delta_s/2)^2}}{\pi \hbar^2 v_s^2} H\left(D_0 + D_s - \frac{\Delta_s}{2} - E\right). \quad \text{(A4b)}$$

Now the 2D concentrations of electrons n and holes p can be calculated as follows:

$$n(E_F) = \int_{-\infty}^{+\infty} g_G^+(E) f(E - E_F) dE$$

$$= \sum_s \int_{-\infty}^{+\infty} \frac{|E - D_0 - D_s|}{\pi \hbar^2 v_s^2} H\left(E - D_0 - D_s - \frac{\Delta_s}{2}\right) f(E - E_F) dE$$

$$= \sum_s \int_{D_0 + D_s + \frac{\Delta_s}{2}}^{+\infty} \frac{|E - D_0 - D_s|}{\pi \hbar^2 v_s^2 \left[1 + \exp\left(\frac{E - E_F}{k_B T}\right)\right]} dE = \left| E - D_0 - D_s - \frac{\Delta_s}{2} \equiv \tilde{E} \right|$$

$$= \sum_s \int_0^{+\infty} \frac{\tilde{E} + \frac{\Delta_s}{2}}{\pi \hbar^2 v_s^2 \left[1 + \exp\left(\frac{\tilde{E} - E_F + D_0 + D_s + \frac{\Delta_s}{2}}{k_B T}\right)\right]} d\tilde{E}$$

$$= \sum_s \left[\frac{\Delta_s k_B T}{2\pi \hbar^2 v_s^2} \ln\left(1 + e^{\frac{E_F - D_0 - D_s - \frac{\Delta_s}{2}}{k_B T}}\right) - \frac{(k_B T)^2}{\pi \hbar^2 v_s^2} \mathrm{Li}_2\left(-e^{\frac{E_F - D_0 - D_s - \frac{\Delta_s}{2}}{k_B T}}\right) \right], \tag{A5a}$$

$$p(E_F) = \int_{-\infty}^{+\infty} g_G^-(E) f(E_F - E) dE = \int_{-\infty}^{+\infty} \sum_s \frac{|E - D_0 - D_s|}{\pi \hbar^2 v_s^2} H\left(D_0 + D_s - \frac{\Delta_s}{2} - E\right) f(E_F - E) dE$$

$$= \sum_s \int_{-\infty}^{D_0 + D_s - \frac{\Delta_s}{2}} \frac{|E - D_0 - D_s|}{\pi \hbar^2 v_s^2 \left[1 + \exp\left(\frac{E_F - E}{k_B T}\right)\right]} dE = \left| D_0 + D_s - \frac{\Delta_s}{2} - E \equiv \tilde{E} \right|$$

$$= \sum_s \int_0^{+\infty} \frac{\tilde{E} + \frac{\Delta_s}{2}}{\pi \hbar^2 v_s^2 \left[1 + \exp\left(\frac{\tilde{E} + E_F - D_0 - D_s + \frac{\Delta_s}{2}}{k_B T}\right)\right]} d\tilde{E}$$

$$= \sum_s \left[\frac{\Delta_s k_B T}{2\pi \hbar^2 v_s^2} \ln\left(1 + e^{\frac{-E_F + D_0 + D_s - \frac{\Delta_s}{2}}{k_B T}}\right) - \frac{(k_B T)^2}{\pi \hbar^2 v_s^2} \mathrm{Li}_2\left(-e^{\frac{-E_F + D_0 + D_s - \frac{\Delta_s}{2}}{k_B T}}\right) \right]. \tag{A5b}$$

Here, we suppose that $\Delta_s > 0$, $\ln(x) \equiv \log_e(x)$, and $\mathrm{Li}_2(x)$ is a particular case of the polylogarithm function $\mathrm{Li}_m(x) = \sum_{k=1}^{\infty}(x^k/k^m)$. These very cumbersome expressions can be essentially simplified into two limiting cases. Namely, we recall the approximate relations, valid in different asymptotic cases,

$$\mathrm{Li}_2(-e^\xi) \cong \begin{array}{ll} e^\xi & \text{at } \xi < 0 \text{ and } |\xi| \gg 1, \\ \frac{\xi^2}{2} & \text{at } \xi > 0 \text{ and } |\xi| \gg 1. \end{array} \tag{A6a}$$

$$\ln(1 + e^\xi) \cong \begin{array}{ll} e^\xi & \text{at } \xi < 0 \text{ and } |\xi| \gg 1, \\ \xi & \text{at } \xi > 0 \text{ and } |\xi| \gg 1. \end{array} \tag{A6b}$$

Using Eq. (A6), one can obtain, from Eq. (A5a), the following expression for the electron concentration, which is valid under the condition $|E_F - D_0 - D_s - (\Delta_s/2)| \gg k_B T$:

$$n(E_F) \cong \sum_s \frac{1}{2\pi \hbar^2 v_s^2} \left[\Delta_s \left(E_F - D_0 - D_s - \frac{\Delta_s}{2}\right) + \left(E_F - D_0 - D_s - \frac{\Delta_s}{2}\right)^2 \right]$$

$$\equiv \sum_s \frac{(E_F - D_0 - D_s)^2 - \left(\frac{\Delta_s}{2}\right)^2}{2\pi \hbar^2 v_s^2} \quad \text{at} \quad E_F > D_0 + D_s + \frac{\Delta_s}{2} \tag{A7a}$$

$$n(E_F) \cong \sum_s \frac{(k_B T)^2}{\pi \hbar^2 v_s^2} \left[\frac{\Delta_s}{2 k_B T} + 1 \right] e^{\frac{E_F - D_0 - D_s - \frac{\Delta_s}{2}}{k_B T}} \quad \text{at} \quad E_F < D_0 + D_s + \frac{\Delta_s}{2}. \tag{A7b}$$

In a similar way, from Eqs. (A5b) and (A6), on can obtain the following expressions for the hole concentration, which is valid under the condition $|-E_F + D_0 + D_s - (\Delta_s/2)| \gg k_B T$:

$$
\begin{aligned}
p(E_F) &\cong \sum_s \frac{1}{2\pi\hbar^2 v_s^2} \left[\Delta_s \left(-E_F + D_0 + D_s - \tfrac{\Delta_s}{2} \right) + \left(-E_F + D_0 + D_s - \tfrac{\Delta_s}{2} \right)^2 \right] \\
&\equiv \sum_s \frac{\left(-E_F + D_0 + D_s\right)^2 - \left(\frac{\Delta_s}{2}\right)^2}{2\pi\hbar^2 v_s^2} \quad \text{at} \quad E_F < D_0 + D_s - \tfrac{\Delta_s}{2}
\end{aligned}
\tag{A8a}
$$

$$
p(E_F) \cong \sum_s \frac{(k_B T)^2}{\pi\hbar^2 v_s^2} \left[\frac{\Delta_s}{2 k_B T} + 1 \right] e^{\frac{-E_F + D_0 + D_s - \frac{\Delta_s}{2}}{k_B T}} \quad \text{at } E_F > D_0 + D_s - \frac{\Delta_s}{2}.
\tag{A8b}
$$

A comparison of Eqs. (A7a) and (A8b) shows that at $E_F > D_0 + D_s + (\Delta_s/2)$ the strong inequality is valid

$$
n(E_F) \gg p(E_F) \quad \text{at} \quad E_F > D_0 + D_s + \frac{\Delta_s}{2},
\tag{A9a}
$$

while at $E_F < D_0 + D_s - (\Delta_s/2)$ the situation is reversed

$$
n(E_F) \ll p(E_F) \quad \text{at} \quad E_F < D_0 + D_s - \frac{\Delta_s}{2}.
\tag{A9b}
$$

Since the determination of the Fermi energy, E_F, requires the calculation of the total charge density, Eqs. (A7)–(A9) allow one to write down the charge density $\rho(E_F) = e[p(E_F) - p(E_F)]$ as

$$
\rho(E_F) \cong
\begin{cases}
\frac{e}{2\pi\hbar^2} \sum_s \frac{(E_F - D_0 - D_s)^2 - \left(\frac{\Delta_s}{2}\right)^2}{v_s^2} \text{sign}(D_0 + D_s - E_F), & |E_F - D_0 - D_s| > \frac{\Delta_s}{2} \\
\sum_s \frac{e(k_B T)^2}{\pi\hbar^2 v_s^2} \left[\frac{\Delta_s}{k_B T} + 2 \right] e^{-\frac{\Delta_s}{2 k_B T}} \sinh\left(\frac{D_0 + D_s - E_F}{k_B T} \right) & |E_F - D_0 - D_s| \ll \frac{\Delta_s}{2}
\end{cases}
\tag{A10}
$$

Assuming that $v_s \approx v_F$, the approximate expression for the Fermi energy should be found from the equation $\rho(E_F) + \sigma = 0$, which is a quadratic equation

$$
E_F^2 - E_F(2D_0 + D_\uparrow + D_\downarrow) + \frac{1}{2}\left[(D_0 + D_\uparrow)^2 + (D_0 + D_\downarrow)^2 - \left(\frac{\Delta_\uparrow}{2}\right)^2 - \left(\frac{\Delta_\downarrow}{2}\right)^2 \right] - \frac{\pi\hbar^2 v_F^2 \sigma}{e} \cong 0.
\tag{A11}
$$

The solution of Eq. (A11) is

$$
\begin{aligned}
E_F(\sigma) &\approx D_0 + \frac{D_\uparrow + D_\downarrow}{2} + \sqrt{ \left(D_0 + \frac{D_\uparrow + D_\downarrow}{2} \right)^2 + \frac{\pi\hbar^2 v_F^2 \sigma}{e} - \frac{1}{2}\left[(D_0 + D_\uparrow)^2 + (D_0 + D_\downarrow)^2 - \left(\frac{\Delta_\uparrow}{2}\right)^2 - \left(\frac{\Delta_\downarrow}{2}\right)^2 \right] } \\
&= D_0 + \frac{D_\uparrow + D_\downarrow}{2} + \sqrt{ \frac{1}{8}\left[\Delta_\uparrow{}^2 + \Delta_\downarrow{}^2 \right] - \left(\frac{D_\uparrow - D_\downarrow}{2} \right)^2 + \frac{\pi\hbar^2 v_F^2 \sigma}{e} }
\end{aligned}
\tag{A12}
$$

It is seen from Fig. 6 that the approximate dependence for the charge density is close to the exact ones.

APPENDIX B: MEAN FREE PATH ESTIMATES

Landauer formula (3) describes the conductance of a perfect graphene channel in the ballistic regime (BR), which can be estimated as [33,34]

$$
G_{\text{BR}} \sim \frac{2e^2}{\hbar\pi^{3/2}} W \sqrt{n_{2D}}.
\tag{B1}
$$

Here, $e = 1.6 \times 10^{-19}$ C is the elementary charge; $\hbar = 1.056 \times 10^{-34}$ J s is the Planck constant; W is the channel width; and n_{2D} is the 2D concentration of carriers, which can be estimated for a single-domain ferroelectric as $n_{2D} \approx |P_3/e|$.
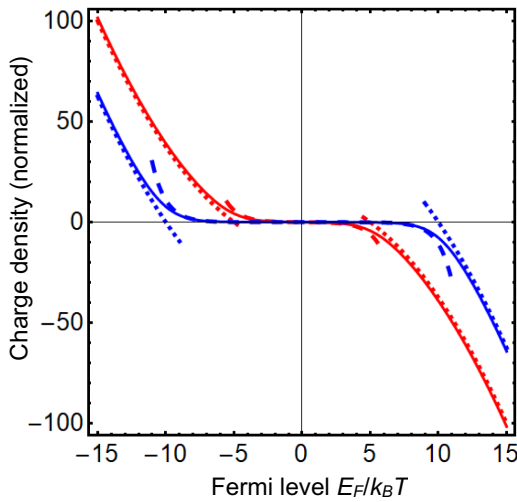
FIG. 6. Total charge density as a function of normalized Fermi level for $\Delta_s/k_B T = 10$ and 20 (red and blue curves, respectively). Solid curves are plotted with exact expressions (A5), while dotted and dashed curves are based on the expressions (7a),(8a) and (7b),(8b), respectively.

Since we use Eq. (3) for room and elevated temperatures in the main text, it is necessary to estimate the hierarchy of electron mean free passes determined by scattering at graphene edges (GE), acoustic phonons (AP), and substrate ionized charged impurities (CI). The resulting electron mean free path λ is [32]

$$\frac{1}{\lambda} = \frac{1}{\lambda_{\text{GE}}} + \frac{1}{\lambda_{\text{AP}}} + \frac{1}{\lambda_{\text{CI}}}. \qquad (B2)$$

As a rule, the scattering at GE leads to the expression for a mean free path contribution

$$\lambda_{\text{GE}} \sim \beta W, \qquad (B3)$$

where W is the channel width, β is an almost-temperature-independent dimensionless factor in the order of two to ten, depending on the type of GE (zigzag or armchair, see, e.g., Ref. [50]) and on the geometry of the problem. Since the inverse value, $1/\lambda_{\text{GE}}$, matters in Eq. (B2), the scattering at GE can dominate only under special conditions (e.g., in the nanoribbon with zigzag edges) and becomes negligibly weak for $W \geq 50$ nm in the case of a graphene channel with $L \sim 100$ nm, as considered in this work.

Scattering at the acoustic phonons is weak because of weak electron-phonon coupling in graphene, and λ_{AP} is in the order of several μm under ambient conditions [32]. The mechanism of scattering at AP can be dominant only in some exotic situations, such as in stretched graphene without its contact with the substrate [34], and thus, can be neglected in the considered case of freely suspended graphene.

Scattering at ionized CI in the substrate is the most common mechanism of carrier scattering in real graphene devices with almost perfect graphene channels containing a very small number of structural imperfections [32]. Its contribution to the mean free path is

$$\lambda_{\text{CI}} \sim \alpha \sqrt{n_{\text{2D}}}, \qquad (B4)$$

where the proportionality coefficient α, which can be treated as the effective CI scattering cross section, has dimensions of nm^2 and depends on the substrate material and graphene-substrate interface chemistry [see Eqs. (3.20)–(3.22) in Ref. [32]]. Therefore, the inequality $\lambda_{\text{CI}} \gg L$, which is required for negligibility of CI scattering, imposes some restrictions on carrier concentration in the graphene channel and ferroelectric polarization, allowing for their temperature dependences. Actually, taking into account that $P_3 \cong P_0\sqrt{1 - [T/T_{\text{PE-FE}_c}(u_m, h)]} \cong 0.5$ C/m^2 at room temperature (see Fig. 3d), but can be several times smaller as the temperature increases to 400–600 K, depending on the film thickness and (compressive or tensile) misfit strain, an elementary estimate gives $n_{\text{2D}} \approx |P_3/e| \cong 3 \times 10^{18}\left\{\sqrt{1 - [T/T_{\text{PE-FE}_c}(u_m, h)]}\right\}$ m^{-2} over the actual temperature range. Thus, scattering at CI becomes unimportant when $\alpha\sqrt{P_0/e}\sqrt[4]{1 - [T/T_{\text{PE-FE}_c}(u_m, h)]} \cong 1.73\alpha\sqrt[4]{1 - [T/T_{\text{PE-FE}_c}(u_m, h)]} \gg L$, where α is taken in nm^2 and L is taken in nm. Since the surface concentration of CI in a ferroelectric substrate is typically much smaller than that of n_{2D} at room and lower temperatures, the inequality $\alpha\sqrt{P_0/e} \gg L$ provides the domination of BR with negligible CI scattering at $L \geq 100$ nm.

Notably, there is no need to change the strain under the valve-filter device operation. The multilayered structure of ferromagnetic-graphene-strained ferroelectric film-substrate is formed only once, during the synthesis of the ferroelectric film. The role of strain is to control the phase-transition temperatures of the ferroelectric film (e.g., effective Curie temperature) and the value of its polarization, which is chosen in such way that the ferromagnetic-graphene-strained ferroelectric film-substrate structure can operate effectively over a given temperature range. This is the very idea of strain engineering, which is successfully used for many ferroelectrics (see, e.g., Ref. [40]).

[1] K. S. Novoselov, A. K. Geim, S. V. Morozov, D. Jiang, Y. Zhang, S. V. Dubonos, I. V. Grigorieva, and A. A. Firsov, Electric field effect in atomically thin carbon films, Science **306**, 666 (2004).

[2] S. Datta, Yongqing Cai, I. Yudhistira, Z. Zeng, Y.-W. Zhang, H. Zhang, S. Adam, J. Wu, and K. P. Loh, Tuning magnetoresistance in molybdenum disulfide and graphene using a molecular spin transition, Nat. Commun. **8**, 677 (2017).

[3] L. Brey and Y. A. Fertig, Magnetoresistance of graphene-based spin valves, Phys. Rev. B **76,** 205435 (2007).

[4] C. Józsa, M. Popinciuc, N. Tombros, H. T. Jonkman, and B. J. Van Wees, Electronic Spin Drift in Graphene Field-Effect Transistors, Phys. Rev. Lett. **100,** 236603 (2008).

[5] S. Ringer, M. Rosenauer, T. Völkl, M. Kadur, F. Hopperdietzel, D. Weiss, and J. Eroms, Spin field-effect transistor action via tunable polarization of the spin injection in a Co/MgO/graphene contact, Appl. Phys. Lett. **113,** 132403 (2018).

[6] Y.-F. Wu, H.-D. Song, L. Zhang, X. Yang, Z. Ren, D. Liu, H.-C. Wu, J. Wu, J.-G. Li, Z. Jia, B. Yan, X. Wu, C.-G. Duan, G. Han, Z.-M. Liao, and D. Yu, Magnetic proximity effect in graphene coupled to a $BiFeO_3$ nanoplate, Phys. Rev. B **95,** 195426 (2017).

[7] Yu. Wicaksono, S. Teranishi, K. Nishiguchi, and K. Kusakabe, Tunable induced magnetic moment and in-plane conductance of graphene in Ni/graphene/Ni nano-spin-valve-like structure: A first principles study, Carbon **143,** 828 (2019).

[8] F. Ibrahim, A. Hallal, D. S. Lerma, X. Waintal, E. Y. Tsymbal, and M. Chshiev, Unveiling multiferroic proximity effect in graphene, 2D Mater. **7,** 015020 (2019).

[9] D. A. Solis, A. Hallal, X. Waintal, and M. Chshiev, Proximity magnetoresistance in graphene induced by magnetic insulators, Phys. Rev. B **100,** 104402 (2019).

[10] A. Hallal, Graphene-based spinmechatronic valve, 2D Mater. **7,** 015005 (2020).

[11] H. X. Yang, A. Hallal, D. Terrade, X. Waintal, and S. Roche, M. Chshiev. Proximity Effects Induced in Graphene by Magnetic Insulators: First-Principles Calculations on Spin Filtering and Exchange-Splitting Gaps, Phys. Rev. Lett. **110,** 046603 (2013).

[12] A. Hallal, F. Ibrahim, H. Yang, S. Roche, and M. Chshiev, Tailoring magnetic insulator proximity effects in graphene: First-principles calculations, 2D Mater. **4,** 025074 (2017).

[13] Y. Song and G. Dai, Spin filter and spin valve in ferromagnetic graphene, Appl. Phys. Lett. **106,** 223104 (2015).

[14] X.-W. Zhang, D. Xie, J.-L. Xu, C. Zhang, Y.-L. Sun, Y.-F. Zhao, X. Li, X.-M. Li, H.-W. Zhu, H.-M. Chen, and T.-C. Chang, Temperature-dependent electrical transport properties in graphene/$Pb(Zr_{0.4}Ti_{0.6})O_3$ field effect transistors, Carbon **93,** 384 (2015).

[15] A. Rajapitamahuni, J. Hoffman, C. H. Ahn, and X. Hong, Examining graphene field effect sensors for ferroelectric thin film studies, Nano Lett. **13,** 4374 (2013).

[16] M. H. Yusuf, B. Nielsen, M. Dawber, and X. Du, Extrinsic and intrinsic charge trapping at the graphene/ferroelectric interface, Nano Lett. **14,** 5437 (2014).

[17] A. I. Kurchak, E. A. Eliseev, S. V. Kalinin, M. V. Strikha, and A. N. Morozovska, p-n Junction Dynamics Induced in a Graphene Channel by Ferroelectric-Domain Motion in the Substrate, Phys. Rev. Appl. **8,** 024027 (2017).

[18] A. I. Kurchak, A. N. Morozovska, E. A. Eliseev, S. V. Kalinin, and M. V. Strikha, Nontrivial temperature behavior of the carrier concentration in graphene on ferroelectric substrate with domain walls, Acta Mater. **155,** 302 (2018).

[19] Y. Zheng, G.-X. Ni, C.-T. Toh, C.-Y. Tan, K. Yao, and B. Özyilmaz, Graphene Field-Effect Transistors with Ferroelectric Gating, Phys. Rev. Lett. **105,** 166602 (2010).

[20] A. I. Kurchak, A. N. Morozovska, and M. V. Strikha, Magnetic dielectric- graphene- ferroelectric system as a promising non-volatile device for modern spintronics, J. Appl. Phys. **125,** 174105 (2019).

[21] N. A. Pertsev, A. G. Zembilgotov, and A. K. Tagantsev, Effect of Mechanical Boundary Conditions on Phase Diagrams of Epitaxial Ferroelectric Thin Films, Phys. Rev. Lett. **80,** 1988 (1998).

[22] A. R. Damodaran, J. C. Agar, S. Pandya, Z. Chen, L. Dedon, R. Xu, B. Apgar, S. Saremi, and L. W. Martin, New modalities of strain-control of ferroelectric thin films, J. Phys.: Condens. Matter. **28,** 263001 (2016).

[23] S. Reich, J. Maultzsch, C. Thomsen, and P. Ordejon, Tight-binding description of graphene, Phys. Rev. B **66,** 035412 (2002).

[24] F. Liu, P. Ming, and J. Li, Ab initio calculation of ideal strength and phonon instability of graphene under tension, Phys. Rev. B **76,** 064120 (2007).

[25] J. L. Lado, N. Garcia-Martinez, and J. Fernandez-Rossier, Edge states in graphene-like systems, Synth. Met. **210,** 56 (2015).

[26] M. O. Groerbig, The quantum hall effect in graphene – a theoretical perspective, , C.R. Phys. **12,** 369 (2011).

[27] D. A. Abanin and L. S. Levitov, Quantized transport in graphene p-n junctions in a magnetic field, Science **317,** 641 (2007).

[28] R. Landauer, Spatial variation of currents and fields Due to localized scatterers in metallic conduction, IBM J. Res. Dev. **1,** 223 (1957).

[29] Y. O. Krugluak and M. V. Strikha. Ukr. J. Phys. Rev. **10,** 3 (2015).

[30] E. V. Gorbar, V. P. Gusynin, V. A. Miransky, and I. A. Shovkovy, Magnetic field driven metal-insulator phase transition in planar systems, Phys. Rev. B **66,** 045108 (2002).

[31] N. F. Mott, Electrons in transition metals, Adv. Phys. **13,** 325 (1964).

[32] S. D. Sarma, S. Adam, E. H. Hwang, and E. Rossi, Electronic transport in two-dimensional graphene, Rev. Mod. Phys. **83,** 407 (2011).

[33] M. V. Strikha and A. N. Morozovska, Limits for the graphene on ferroelectric domain wall p-n-junction rectifier for different regimes of current, J. Appl. Phys. **120,** 214101 (2016).

[34] A. N. Morozovska, A. I. Kurchak, and M. V. Strikha, Graphene Exfoliation at Ferroelectric Domain Wall Induced by Piezoeffect: Impact on the Conduction of Graphene Channel, Phys. Rev. Appl. **8,** 054004 (2017).

[35] M. Koch, F. Ample, C. Joachim, and L. Grill, Voltage-dependent conductance of a single graphene nanoribbon, Nat. Nanotechnol. **7,** 713 (2012).

[36] A. N. Morozovska, A. S. Pusenkova, O. V. Varenyk, S. V. Kalinin, E. A. Eliseev, and M. V. Strikha, Finite size effects of hysteretic dynamics in multi-layer graphene on ferroelectric, Phys. Rev. B **91,** 235312 (2015).

[37] A. K. Tagantsev, G. Gerra, and N. Setter, Short-range and long-range contributions to the size effect in metal-ferroelectric-metal heterostructures, Phys. Rev. B **77,** 174111 (2008).

[38] J. Wang, A. K. Tagantsev, and N. Setter, Size effect in ferro-electrics: Competition between geometrical and crystalline symmetries, Phys. Rev. B **83**, 014104 (2011).

[39] M. V. Strikha, A. I. Kurchak, and A. N. Morozovska, Integer quantum hall effect in graphene channel with p-n junction at domain wall in ferroelectric substrate, J. Appl. Phys. **125**, 082525 (2019).

[40] C. Ederer and N. A. Spaldin, Effect of Epitaxial Strain on the Spontaneous Polarization of Thin Film Ferroelectrics, Phys. Rev. Lett. **95**, 257601 (2005).

[41] M. J. Haun, Z. Q. Zhuanga, E. Furman, S. J. Jang, and L. E. Cross, Thermodynamic theory of the lead zirconate-titanate solid solution system, part III: Curie constant and sixth-order polarization interaction dielectric stiffness coefficients, Ferroelectrics **99**, 45 (1989).

[42] W. Han, R. K. Kawakami, M. Gmitra, and J. Fabian, Graphene spintronics, Nat. Nanotechnol. **9**, 794 (2014).

[43] E. I. Rashba and V. I. Sheka, Fiz. Tverd. Tela – Collected Papers (Leningrad), v.II, 162-176 (1959) (in Russian), English translation: Supplemental Material to the paper by G. Bihlmayer, O. Rader, and R. Winkler, Focus on the Rashba effect, New J. Phys. 17, 050202 (2015).

[44] A. Fert and I. A. Campbell, Two-current Conduction in Nickel, Phys. Rev. Lett. **21**, 1190 (1968).

[45] A. H. Castro Neto, F. Guinea, N. M. R. Peres, K. S. Novoselov, and A. K. Geim, The electronic properties of graphene, Rev. Mod. Phys. **81**, 109 (2009).

[46] H. Yang, Significant dzyaloshinskii–moriya interaction at graphene–ferromagnet interfaces due to the rashba effect, Nat. Mater. **17**, 605 (2018).

[47] A. K. Tagantsev, L. E. Cross, and J. Fousek, *Domains in Ferroic Crystals and Thin Films* (Springer, New York, 2010).

[48] S. V. Kalinin, Y. Kim, D. Fong, and A. N. Morozovska, Surface-screening mechanisms in ferroelectric thin films and their effect on polarization dynamics and domain structures, Rep. Prog. Phys. **81**, 036502 (2018).

[49] J. M. Gregg, Exotic domain states in ferroelectrics: Searching for vortices and skyrmions, Ferroelectrics **433**, 74 (2012).

[50] V. K. Dugaev and M. I. Katsnelson, Edge scattering of electrons in graphene: Boltzmann equation approach to the transport in graphene nanoribbons and nanodisks, Phys. Rev. B **88**, 235432 (2013).